applied sciences

MDPI

Article

Automated Quantification of Raster Orientation of Fused Filament Fabrication Components Using Ultrasonic Testing

Atik Amin, David A. Jack and Trevor J. Fleck *

Department of Mechanical Engineering, Baylor University, Waco, TX 76798, USA; david_jack@baylor.edu (D.A.J.)
* Correspondence: trevor_fleck@baylor.edu

Abstract: An automated method for nondestructively characterizing the layer-by-layer raster orientation of additively manufactured components fabricated via the fused filament fabrication (FFF) process is presented, which utilizes full waveform capture of the ultrasonic signal paired with two-dimensional fast Fourier transform analysis. The proposed method extracts internal features of the fabricated component at various depths and then applies the two-dimensional Fourier transformation in the spatial domain to analyze the raster path and extract the orientation. Three material systems are studied: a standard polymer (Poly cyclohexylenedimethylene terephthalate glycol, PCTG), an engineered polymer (high-temperature nylon, HTN) and a carbon fiber-filled polymer (polyethylene terephthalate, PET-CF). Samples were fabricated using an industrial-grade FFF system and scanned using a high-resolution custom immersion ultrasonic platform. Studies were performed using both a 10 MHz and a 15 MHz spherically focused transducer, with the 10 MHz transducer yielding more accurate and more consistent results for the investigated material systems. The analyzed results show that the presented automated method can accurately identify the direction of the raster path with an error within 1°–2° in each of the first 9~10 deposited layers of the investigated PCTG and the PET-CF samples, and the first 14 layers of the HTN samples. This study provides an approach for the automated analysis of the internal features of FFF components using ultrasonic testing, which can further inform the quality control process, in turn increasing reliability and enabling acceptance of AM parts in various industries.

Keywords: additive manufacturing; fused filament fabrication; nondestructive evaluation; raster orientation; ultrasonic testing

Citation: Amin, A.; Jack, D.A.; Fleck, T.J. Automated Quantification of Raster Orientation of Fused Filament Fabrication Components Using Ultrasonic Testing. *Appl. Sci.* **2024**, *14*, 4769. https://doi.org/10.3390/app14114769

Academic Editor: Piero Tortoli

Received: 1 May 2024
Revised: 20 May 2024
Accepted: 23 May 2024
Published: 31 May 2024

1. Introduction

Additive manufacturing (AM) is gathering significant interest in a variety of industries, such as aerospace, automotive, and medical, among many others. Fused filament fabrication (FFF), or fusion-based material extrusion additive manufacturing, is one of the most common methods of AM for producing functional polymer and polymer composite AM components. Due to its increased application and use in industry, the quality and performance of the manufactured component have become increasingly important factors. To date, the mechanical performance of FFF components has proven to be inferior to traditionally manufactured components, with a significant contributing factor being the reliability concerns from part to part. The development and use of nondestructive testing (NDT) technologies, tuned for FFF components, will further enable the use of FFF components in critical, end-use applications. The work herein garners insights into the nondestructive testing of FFF components, providing an effective means of estimating component performance using ultrasonic testing (UT) to quantify the internal, as-manufactured, raster orientation layer-by-layer.

Process parameters, one of the most significant being the raster orientation, have been shown to have a significant impact on the final component performance [1,2]. The orientation of the internal raster path, or raster orientation, of an FFF component refers

to the direction of material deposition, with respect to a given axis within the FFF printer, which often varies layer by layer. Sood discussed that small raster angles offer more resistance to flexural strength and failure as the deposited rasters are more aligned along the load direction, resulting in improved strength [2]. Research indicates raster orientation plays a fundamental role in determining the mechanical properties of additively manufactured components [3,4]. Among the numerous works investigating the effects of raster orientation, Wu et al. [3] explored the impact of varying raster orientations, including $0^\circ/90^\circ$, $30^\circ/-60^\circ$, and $45^\circ/-45^\circ$, on the mechanical properties of a 3D-printed polyether-ether-ketone (PEEK) by testing their tensile, compressive, and bending strength. The highest tensile strength recorded was 56.6 MPa with the $0^\circ/90^\circ$ orientation when the filaments were aligned parallel to the load direction. The tensile strengths of 41.8 MPa and 43.3 MPa were noted when the raster orientations were $30^\circ/-60^\circ$ and $45^\circ/-45^\circ$. Several additional studies have highlighted the substantial influence of raster orientation on the tensile strength of additively manufactured parts [5,6]. Acrylonitrile Butadiene Styrene (ABS) test coupons fabricated with 0° and 90° orientations, respectively, underwent the tensile test procedure, resulting in a decrease in the ultimate strength ranging from 81% to 26% [5]. Rajni et al. [7] conducted additional investigations on the influence of raster orientations on the mechanical properties of 3D-printed PLA specimens. Their findings proved $45^\circ/-45^\circ$ oriented specimens exhibited a 41.20% increase in impact strength compared to those specimens oriented at $0^\circ/90^\circ$.

Several dogbone specimens featuring $45^\circ/-45^\circ$ and $0^\circ/90^\circ$ raster orientations manufactured with ABS were subjected to fatigue analysis [8]. It was observed with the increasing percentage of mean ultimate tensile strength that both orientations failed at an equivalent number of cycles. On the other hand, when subjected to identical absolute stress levels, the $45^\circ/-45^\circ$ orientation exhibited an increased number of cycles to failure by 63.5%. In addition to affecting the strength of the object, raster orientation influences the fracture mechanism as well [9–11]. Lorenzo-Bañuelos et al. [9] observed the influence of raster orientation on the fracture mechanism of FFF components by incorporating varying raster orientations at different layers. Four scenarios were developed, featuring 0°, 90°, 45°, and -45° orientations, and it was observed that the fracture energy of the specimen prepared with $0^\circ/45^\circ/90^\circ/-45^\circ$ orientations was decreased by 34% compared to the specimens prepared with $45^\circ/-45^\circ$ orientations. Diversities in raster orientations not only impact the strength and fracture of the component but also its toughness. One study found the toughness to be increased by more than 500% when the raster orientations are switched from $[0^\circ/90^\circ]_5$ to $[45^\circ/-45^\circ]_5$ [12]. Srinivasan et al. [13] also performed tensile and fracture toughness tests with raster angles ranging from 0° to 90° with an increment of 15°, where the maximum fracture toughness was observed at 0° and 60°. It is reported in their study that a change in raster angle from 0° to 15° reduced the tensile strength by 22% and toughness by 19%. An important feature of crack alignment was noticed by Khosravani [14], in which crack propagation aligned with the raster orientation for all samples with the exception of those printed with a 0° raster orientation. Prajapati et al. [15] introduced a method of mitigating the loss in final part performance by incorporating thermal annealing process. They mentioned that due to varying orientations in different layers of an additively manufactured component, reduced material characteristics are observed. Yap et al. [16] investigated how raster orientation impacts the elastic properties of PC-ABS material. They developed a method using ultrasound to characterize the change in the sound velocity from various angles relative to the plane of the fabricated component, from which they were able to extract the orthotropic stiffness tensor components. Their results for the bulk orthotropic stiffness tensor components were quite satisfactory, with an average of 11% deviations of the various components from those of structural testing.

Each of the aforementioned studies indicates that raster orientation significantly influences part performance. A similar effect has been noted for traditional laminated CFRPs, in which Rahul et al. [17] in their experiments with composite laminates investigated the effective stiffness, which varied from 47 GPa to 54 GPa for a 2° change in the quantification

of ply orientation using the ultrasound technique. Just as raster orientation affects the final part performance, ply orientation similarly influences the tensile and flexural strengths of carbon/epoxy laminates [18]. Different stacking sequences, including unidirectional, cross-ply, and quasi-isotropic laminates, were subjected to bending, tension, and impact forces, according to the ASTM standards, and it was observed for symmetric cross-ply laminates that flexural and tensile moduli were improved by 59.5% and 3.97%, respectively. Vasudevan et al. [19] investigated the mechanical properties of composite laminates of Kevlar fibers combined with glass fibers for various orientations ranging from 0° to 60°. Their findings indicate that the hybrid composites fabricated with Kevlar fibers oriented at 0° demonstrate a higher tensile strength (327 MPa) as well as flexural strength (390 MPa) compared to the composites with Kevlar fibers oriented at 30°, 45°, and 60°. In addition to examining the composite laminate strength containing different ply orientations, several studies have investigated the failure mechanisms. Ramezani et al. [20] observed in their experiments that thin-plied laminates exhibit reduced levels of failure under out-of-plane loading compared to angle plied CFRPs. Specifically, it was found that the stacking sequence [0°/90°] demonstrated a lower level of failure compared to [45°/−45°] for both CFRP and thin-ply configurations. Another study [21] focused on failure mechanisms, which involved subjecting the thin-ply CFRP laminates to tensile loading. Initially, experiments were conducted to assess the tensile behavior of 15° and 30° ply angles, and finally, FEM models were developed to anticipate the failure mode. The failure strains for the mentioned ply angles varied depending on the different fiber areal weights. Specifically, when the ply angle was 15°, the failure strains were 1.187%, 1.35%, and 1.22% for corresponding areal weights of 20, 60, and 120 g/m^2. In contrast, when the ply angle was 30°, the failure strains were 3.52%, 4.94%, and 2.9% for the same areal weights.

As such, numerous efforts have sought to quantify the orientation of CFRP laminates using nondestructive evaluation (NDE) in an automated fashion. It should be noted that works related to NDE for the orientation of layered materials to date have been primarily limited to CFRP laminates as opposed to AM components, which is the focus of this work. One of the most notable works was performed by Smith [22], where he investigated the orientation of plies within a unidirectional CFRP skin over a honeycomb sandwich structure. Two techniques were applied to ascertain the ply stacking arrangements. The initial method utilized a portable scanner for the ultrasonic scanning of composites, while the second method required the capture of the full waveform at each point in the scan, the latter of which could effectively distinguish the ply orientations of 0°, 45°, and 90°. Hsu et al. [23] enhanced the automation process of stacking sequences by employing the 2D FFT method to examine the ply orientation of CFRP laminates. C-scan images were generated using the longitudinal wave that extracted fiber orientation information. Their laboratory experiments demonstrated the feasibility of determining the fiber orientations by up to 20 plies. In another study [24], evaluating layup configuration, Hsu used a contact-mode ultrasonic transducer with shear waves to deduce the percentages of 0° and 90° oriented plies from 24 groups of [0°/90°] plies. Smith et al. [25] developed a tool titled StackScan^{TM} to automate the process of arranging ply stacking sequences. This tool provided an accelerated method to detect exact ply orientations with an error margin of 0.5°. Ambrozinski et al. [26] demonstrated how laser ultrasound systems can be employed to detect variations in the ply alignment of composites. In this method, the laser-generated ultrasound signals were used to produce B-scans with a minimal amount of interference, facilitating the visualization of individual plies. However, due to the strong attenuation of the signal in layered composites, significant signal loss occurs at depths exceeding 7–10 mm. Another investigation of CFRP laminates investigated the heating pattern in such composites, determining them to be influenced by fiber orientations [27]. To explore this unique heating behavior, orientations of carbon fiber laminates were assessed using the 2D FFT method of the captured transient thermal surface distributions, leading to the conclusion that thermography can be implemented on specimens consisting of 12 layers to

identify fiber orientations, with the maximum error compared to the designed orientation of 6°.

The present study of automating the raster orientation process from the captured waveform is an extension of the earlier study by the current authors [28,29] that presents a manual approach to identify the raster orientation in a layer-by-layer manner. The study illustrated in this article expands on the methodology proposed in Blackman et al. [30], where a conventional immersion-based ultrasonic system was used to inspect laminated composites. The researchers in the earlier study determined the lamina orientations of fabricated composites with thicknesses ranging from 3 lamina to 18 lamina. The work presented herein focuses on a method for identifying the internal raster orientation using non-destructive means, which would offer valuable insights into the material properties of an unknown part. The authors utilized an ultrasonic NDE method to discern the internal geometrical features. FFF coupons were prepared using a range of functionally viable materials, which were subsequently inspected using conventional, immersion-based UT. An automated algorithm was then presented to analyze the UT data, effectively quantifying the internal raster orientation. The outcomes obtained from the algorithm can expedite additional tasks, such as evaluating mechanical properties associated with raster orientation.

2. Materials and Methods

2.1. Selection of Material and Manufacturing

To automate the process of raster orientation analysis, this study uses components prepared on an industrial-scale FFF machine (Essentium HSE 180-HT, Pflugerville, TX, USA) with a nozzle diameter of 0.8 mm. The parts have a planar dimension of 76.2 mm × 76.2 mm (3 inches × 3 inches) and a height of 6.35 mm (0.25 inches). Simplify 3D (Cincinnati, OH, USA) software version 4.0 was used to slice the CAD model, with the pertinent infill parameters shown in Table 1, specifically the orientation θ_i of each of the individual layers. All layers were set to a layer height of 0.35 mm and 100% infill. The print speed was set to 100 mm/s, and the nozzle temperature was set to 340 °C. This study used three materials: polycyclohexylenedimethylene terephthalate glycol (PCTG), carbon fiber-filled polyethylene terephthalate (PET-CF), and high-temperature-grade nylon (HTN) manufactured by Essentium. Nine coupons were manufactured across the three materials, categorized into three groups (A, B, or C) based on their raster orientation layup, as shown in Table 1. The orientations were selected to mitigate warping while avoiding internal reflections from repeated layers. The material properties of the three inspected materials are presented in Table 2. These properties have been sourced from the manufacturer's technical datasheet [31–33], along with the as-deposited density of the printed components.

Table 1. Layer orientation parameters.

Sample Group	Print Orientation θ_i (in Degrees) $[\theta_1,\theta_2,\ldots,\theta_{18}]$
A	[0,90,10,100,20,110,30,120,40,130,50,140,60,150,70,160,80,170]
B	[0,90,10,100,20,110,30,120,40,130,50,140,60,150,70,160,80,170]
C	[0,90,45,135,20,110,70,160,50,140,85,175,25,115,10,100,110,180]

Table 2. Material properties.

Material	Density (g/cc^3)	As-Printed Density (g/cc^3)	Modulus of Elasticity (GPa)	Chemical Formula
PCTG	1.23	1.17	1.81	$(C_{10}H_8O_4)_n$
HTN	1.20	1.15	3.18	$(C_6H_{11}NO)_n$
PET-CF	1.40	1.32	9.38	$(C_{10}H_8O_4)_n$

2.2. Experimental Setup for Ultrasonic Testing

In this work, a custom immersion ultrasonic system was used for all ultrasonic testing and inspection. The setup with a sample in the immersion tank is shown in Figure 1. Signal generation and digitization of the captured waveform were performed using a Focus PX pulser/receiver (Olympus, Evident Corporation, Tokyo, Japan), operating in full-waveform data capture mode at a 100 MHz digitization rate. Translation was performed using positional stages (Velmex, Bloomfield, NY, USA) that raster the ultrasonic transducer over the component in the x_1 and x_2 directions. The 12.7 mm element diameter transducers in the present study all had a nominal focal length of 38.1 mm (1.5 inches), and testing was completed in a pulse-echo configuration. Based on the work in this study, it was found that a transducer frequency of 10 MHz (nominal 0.4 mm diameter spot size) yielded the highest quality data sets and, therefore, will be the focus of the majority of the experiments. However, it should be noted that 15 MHz (nominal spot size of 0.3 mm) spherically focused transducers were also explored. Coupons were aligned in the (x_1, x_2) coordinate system using the fixture shown in Figure 1. The spherically focused transducer was focused on the midplane of the FFF coupons, using an estimated speed of sound of water, PCTG, PET-CF, and HTN as, respectively, 1480 m/s, 2333 m/s, 2258 m/s, and 2593 m/s. The speed of sound through PCTG, PET-CF, and HTN was measured using the time of flight of the signal. The scanning system was set to a raster size of 0.1 mm in both the x_1 and the x_2 directions, as shown in Figure 1, with all movements managed by a custom software interface created in the MATLAB environment. The choice of 0.1 mm was selected less than the spot size of the transducers, so that the determining factor of resolution was from the available transducer elements.

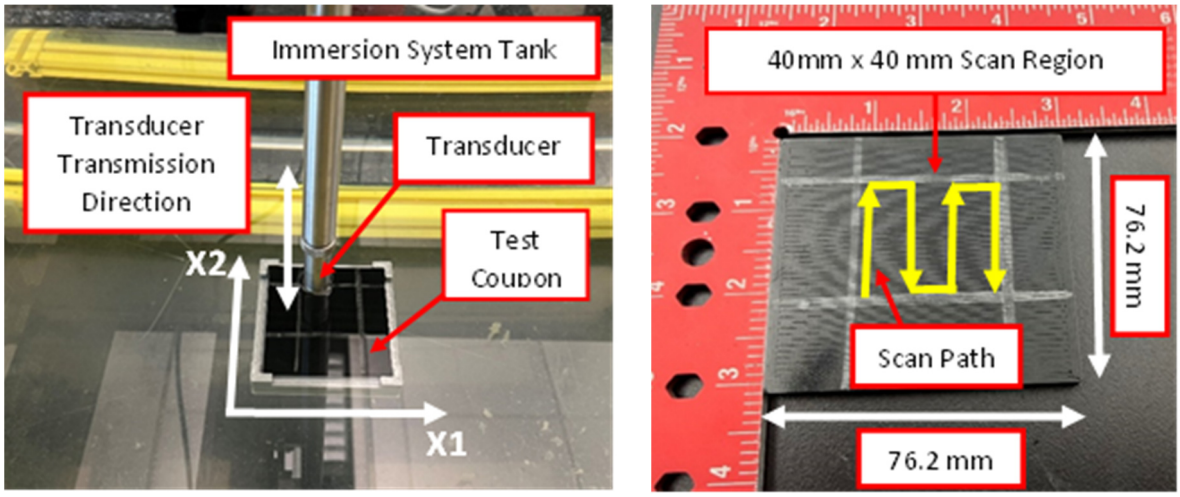

(**a**) (**b**)

Figure 1. Images of (**a**) a representative component with $\times_1$ and $\times_2$ directions and (**b**) a depicted scan path and dimensions of the component.

3. Analysis

To quantify the visualized raster orientation, an in-house MALAB script was used to analyze the fully captured acoustic waveform. The raster was determined with respect to the index direction, labeled x_1 in Figure 1. Data were taken at N_1 discrete points in $x_1 \in \{0, L_1\}$ and N_2 discrete points in $x_2 \in \{0, L_2\}$ that were equally spaced such that $\Delta x_1 = x_{1,j+1} - x_{1,j}$ for all $j \in \{1, 2, \ldots, N_1\}$ and $\Delta x_2 = x_{2,k+1} - x_{2,k}$ for all $k \in \{1, 2, \ldots, N_2\}$. The digitized signal corresponding to the acoustic waveform was defined as $F(t_i, x_{1,j}, x_{2,k})$ where t_i, $x_{1,j}$, and $x_{2,k}$ are discrete values in, respectively, time t, the index direction (x_1), and the scan direction (x_2). In the present study, a 100 MHz digitizer was utilized; thus

$t_{i+1} - t_i = \frac{1}{100\ \text{MHz}} = 10$ ns, and a raster step size of $\Delta x_1 = \Delta x_2 = 0.1$ mm was used. The data were shifted in time such that

$$\widetilde{t}(t, x_1, x_2) = t - t_0(x_1, x_2) \tag{1}$$

where $t_0(x_1, x_2)$ refers to the time at which the initial front wall echo was received by the transmitting transducer. This time shift has the effect of aligning each A-scan in time in reference to the front wall echo at each (x_1, x_2) location, resulting in the array $F\left(\widetilde{t}(t, x_1, x_2), x_{1,k}, x_{2,l}\right)$. Next, a Gaussian smoothing technique was used such that

$$\hat{F}\left(t, x_{1,j}, x_{2,k}\right) = \frac{1}{2\pi\sigma_{x_1}\sigma_{x_2}} \int_{-\infty}^{\infty}\int_{-\infty}^{\infty} e^{\frac{-\left(\widetilde{x}_1 - x_{1,j}\right)^2}{2\sigma_{x_1}^2}} e^{-\frac{\left(\widetilde{x}_2 - x_{2,k}\right)^2}{2\sigma_{x_2}^2}} F\left(\widetilde{t}\left(t, \widetilde{x}_1, \widetilde{x}_2\right), \widetilde{x}_1, \widetilde{x}_2\right) d\widetilde{x}_1 d\widetilde{x}_2 \tag{2}$$

where the distribution parameters σ_{x_1} and σ_{x_2} define the extent of the spatial smoothing of the captured acoustic signal. In the present study, σ_{x_1} and σ_{x_2} were set to three times the raster spacing, specifically 0.3 mm. It was found that 0.3 mm yielded acceptable results without loss of the individual raster features.

Next, a spatially averaged signal $\overline{F}(t)$ was created as

$$\overline{F}(t) = \frac{1}{L_1 L_2} \int_0^{L_2}\int_0^{L_1} \hat{F}(t, x_1, x_2) dx_1 dx_2 \tag{3}$$

A typical result of the spatially averaged signal is shown in Figure 2. Notice in this figure that individual peaks can be observed, with the peak around $t = 0$ corresponding to the front wall reflection of the part and the peak near $t = 6$ µs corresponding to the backwall reflection of the part. From the averaged acoustic signal shown in Figure 2a, the time at which the individual N local maxima of $\overline{F}(t)$ occur can be identified. Except for the front wall and the back wall, each of the observed local maxima are caused by the acoustic reflection of the interface between the individual deposited layers, with a couple of notable exceptions discussed herein. The most relevant exceptions are the peaks near the front surface of the part, i.e., the second and third peaks near $t = 0.5$ µs and $t = 0.7$ µs seen in Figure 2a. This occurs due to the mode shape change of the transmission frequency of the transducer near 10 MHz and the natural frequency caused by the repeated layers that drive the frequency toward 6 MHz in the present study. This mode shape shift causes peaks in the reflected acoustic waveform that do not necessarily correspond to an interface between layers. As such, peaks closer than the known layer height were discarded in the present analysis but will be noted in the report. In practice, any peaks that were closer than one-half of the expected peak-to-peak separation from the designed raster height of 0.35 mm were removed. This yields an array of time values t_n^* for the N layer interfaces and the back wall where $n \in \{1, 2, \ldots, N\}$.

Next, a spatial C-scan was defined for each of the time values t_n^* as

$$C_n(x_1, x_2) = \int_{\widetilde{t}_n}^{\widetilde{t}_n + \Delta t_n} \hat{F}(t, x_1, x_2)^2 dt \tag{4}$$

where the parameter $\widetilde{t}_n$ was a function of the interface time value t_n^*. It was found that using $\widetilde{t}_n = t_n^*$ was ineffective as both the $n-1$ and the n layer reflections were in the reflected signal simultaneously. Selecting the parameter $\widetilde{t}_n$ as

$$\widetilde{t}_n = t_n^* - \delta \tag{5}$$

where $\delta = 40$ ns, which was appropriate for analyzing the n^{th} layer in this work. In general, the parameter Δt_n in Equation (4) was selected to capture as much of the acoustic energy of the reflections from the nth layer as possible without including signal transmission from a previous and/or subsequent layer reflection. For the work herein, $\Delta t_n = \frac{2}{3}\left(t^*_{n+1} - t^*_n\right)$ was found to be sufficient for the analysis, but additional work could be performed to optimize this parameter. This approach allows for adjusting Δt_n in each layer, as not all layers have an equal acoustic width due to the mode conversions of the waveform in the initial signal reflections. A representative example of the spatial C-scan $C_n(x_1, x_2)$ is shown in Figure 3a for the third layer of a scan of part A made from PCTG, a designed 10 degree orientation state.

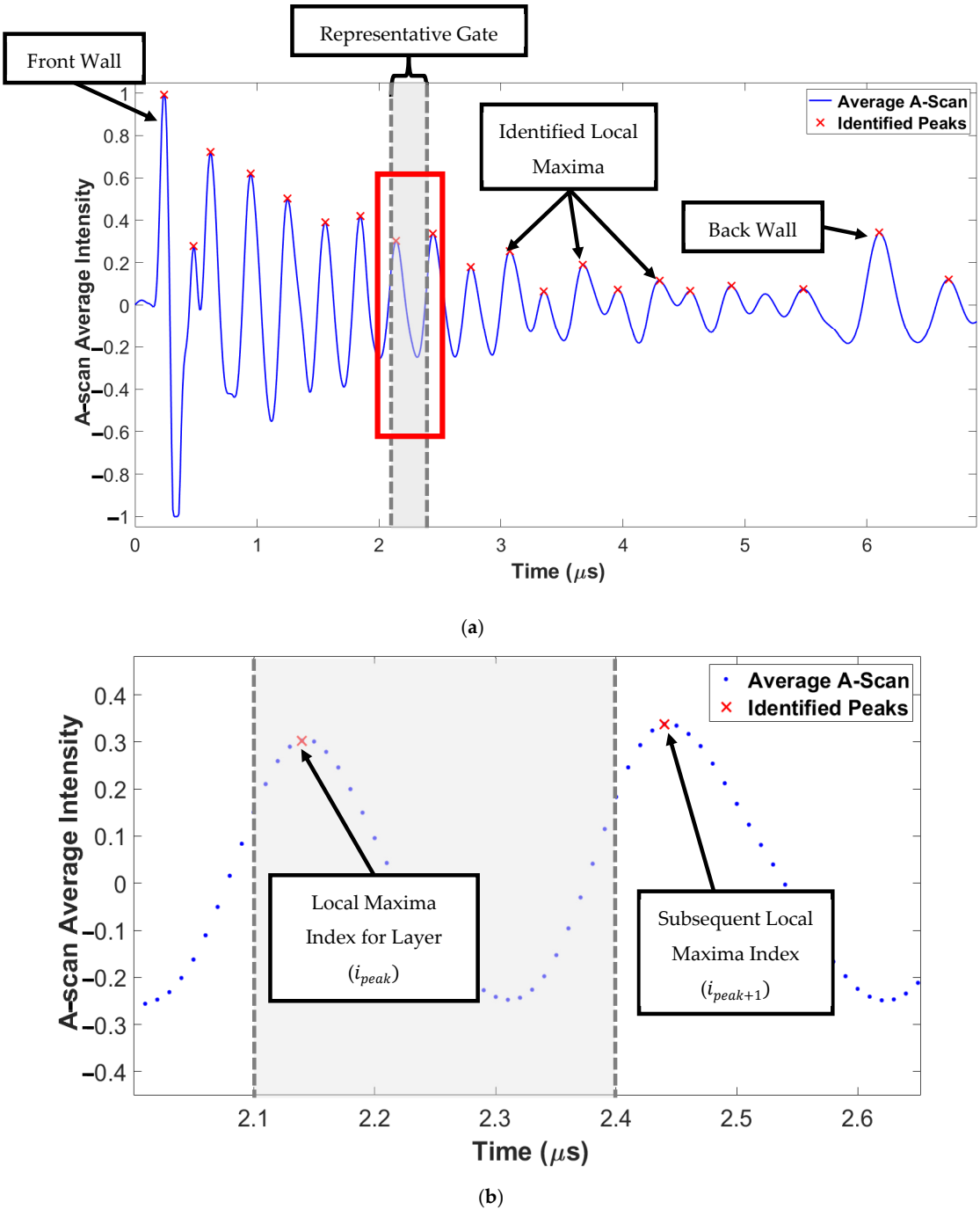

Figure 2. (**a**) Representative A-scan showing gating in time; (**b**) enlarged portion of the representative A-Scan depicted in (**a**).

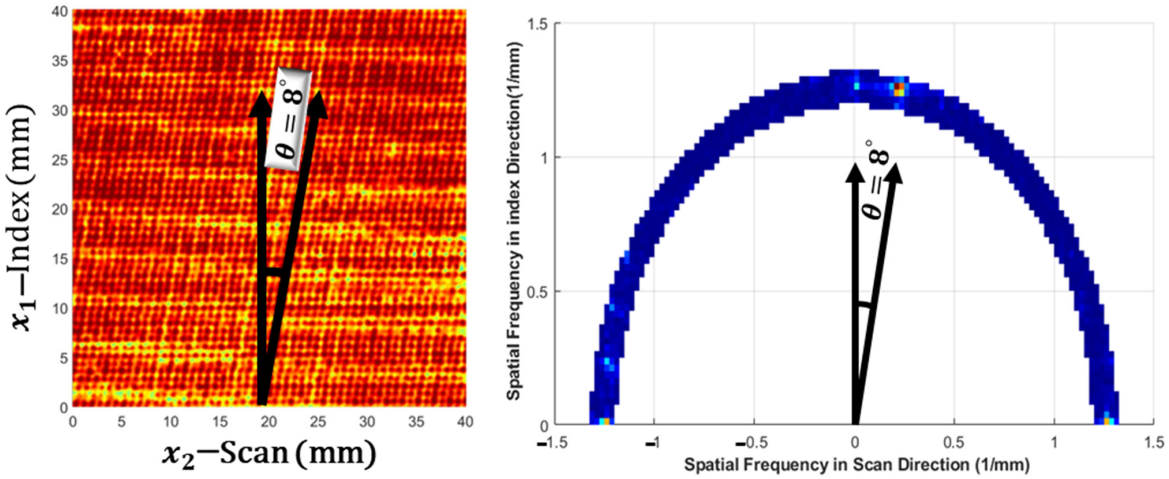

(**a**) (**b**)

Figure 3. PCTG sample at the third layer of part A: (**a**) representative C-scan with (**b**) the associated 2D FFT spectrum with filtering.

Next, a two-dimensional Fourier transform was used to automate of the analysis of the raster orientation. The two-dimensional Fourier transform is defined as

$$\mathcal{C}_n(\omega_1, \omega_2) = \int_0^{L_2} \int_0^{L_1} C_n(x_1, x_2) e^{-i\omega_1 x_1 - i\omega_2 x_2} dx_1 dx_2 \tag{6}$$

where i is the complex number $\sqrt{-1}$. The two-dimensional Fourier transform yielded a signal $\mathcal{C}_n(\omega_1, \omega_2)$ that was originally in the spatial domain (x_1, x_2) and cast it in the spatial frequency space (ω_1, ω_2). The interpretation of the spatial frequency is that the values for (ω_1, ω_2) correspond to the periodicity of features within a two-dimensional space. The specific interest in the present study is the rastered depositions. For example, the individual rows of rasters of the third layer of part A_01 can be observed in Figure 3a. The angle in the (ω_1, ω_2) plane of $\mathcal{C}_n(\omega_1, \omega_2)$ corresponds to the angle at which the rasters are orientated, whereas the magnitude $\overline{\omega} = \sqrt{\omega_1^2 + \omega_2^2}$ of a given peak corresponds to the spatial frequency of a periodic feature of the spatial C-scan, $C_n(x_1, x_2)$. To aid in the automatic feature extraction, a simple band-pass filter in the frequency space was utilized. This was performed by taking the as-designed deposition width of 0.8 mm and removing spatial frequencies from $\frac{1}{0.8\text{ mm}} = 1.25\text{ mm}^{-1}$ in the Fourier domain $\mathcal{C}_n(\omega_1, \omega_2)$. This is shown in Figure 3b, where it was found that a band of $\frac{1}{0.9\text{ mm}}$ to $\frac{1}{0.7\text{ mm}}$ was sufficient in the present study, but this band could be further optimized in future studies. The results of the transform $C_n(x_1, x_2)$ with the bandpass filter imposed for the third layer of part A made from PCTG are shown in Figure 3b. The peak of the signal at 8 degrees is shown, which is identical to the visually determined alignment state in Figure 3a in the spatial domain.

4. Results and Discussion

The first investigation presented here is of the PCTG part A, with the orientation state defined in Table 1. Using the approach outlined in the previous section for the automated raster orientation extraction, the extracted orientation state is presented for the first 10 of the 18 layers in Table 3. Two different scan results are exhibited, the first with a 10 MHz spherically focused transducer and the second with a 15 MHz spherically focused transducer, both with a nominal 38 mm focal length. Observe, in comparison with Table 1, that the orientation for each layer is consistent with a typical error of 0 degrees or 1 degree for each of the captured layers. Analysis after the 10th layer was not performed as the reflection wave signal-to-noise ratio was insufficient for analysis, causing significant

errors in the analysis due to signal attenuation and scatter from the previous layers. It is worth noting that the scan with the 10 MHz transducer yields the 10th layer, whereas the results from the 15 MHz transducer could not penetrate the 10th layer with an acceptable signal-to-noise ratio.

Table 3. Raster orientation up to 10th layer of PCTG part A scanned with a mean transducer frequency of 10 and 15 MHz.

	Layer #									
Frequency	**1**	**2**	**3**	**4**	**5**	**6**	**7**	**8**	**9**	**10**
10 MHz	0 *	90	8	99	19	110	29	119	38	129
15 MHz	0	90	9 *	100	19	110	29	120	39	---

Several numbers in Table 3 have an asterisk (*). This is used to indicate where a layer was ignored, as discussed in the methodology section, due to peaks being too close in time due to the mode shift caused near the front wall. Based on the results from Table 3, along with other in-house studies, the 10 MHz transducer was selected for all the remaining analyses.

The scanning and analysis process was repeated for all three sample types, A, B, and C from Table 1, for each of the three material systems using the 10 MHz transducer for scanning. To assess the accuracy of the automated raster orientation algorithm from Section 3, the error of the nth layer is defined as

$$Error_n = \left| \theta_{designed,n} - \theta_{UT\ Observed,n} \right| \quad (7)$$

where the error will be in units of degrees. A relative error was not used in the current study as the designed orientation ranges from 0 degrees to 180 degrees. The error is plotted in Figure 4 for the type A parts of each of the three material types. Notice that for the first 9 or 10 layers, the error was 0, 1, or 2 degrees for the unfilled polymers as well as the carbon fiber-filled polymer. For the unfilled PCTG polymer and the fiber-filled PET polymer after the 10th layer the orientation state cannot be identified due to a poor signal-to-noise ratio. Conversely, for the engineered polymer HTN, the orientation state can be identified for 17 of the 18 layers in sample type A. Notice that the error in all cases is 2 degrees or less, with the majority of the automated layer orientation extraction yielding an error of 1 degree or 0 degrees.

The process was continued for both part types B and C, and the results are shown in Figure 5. As with part type A, the error was 0, 1, or 2 degrees. Similar to part type A, layers up to the 9th or 10th layer can be identified for all three material systems, but more layers can be identified for the HTN samples. Unlike part type A, the algorithm failed to identify the second layer in the HTN and PCTG samples for both the type B and C parts. Otherwise, the algorithm was successful in identifying the remaining layers up to the 9th layer for the PCTG and the 14th layer for the HTN. Unlike the type A part with HTN, the analysis of the HTN type B and C samples was successful to only the 14th layer. It was observed that with some adjustments of the various parameters, such as δ in Equation (5) or the relative size of Δt_n in Equation (4), various layers could be identified. The optimal setting of these parameters has been left for a future study. It is interesting to note that the accuracy was consistent for the first 9 or 10 layers for each of the material systems, but for the engineered polymer without fiber fill, the signal-to-noise ratio was sufficiently deeper into the part, allowing for the analysis up to the 14th layer (type B and C) and the 17th layer (type A). This additional penetration is likely caused by the highly elastic nature of the viscoelastic HTN material, relative to PCTG, at room temperature, allowing for less attenuation of the signal. The PET-CF sample, with the carbon fiber, will tend to cause considerable scatter; thus, it is not surprising that the penetration of the acoustic signal would be diminished for the fiber-filled system.

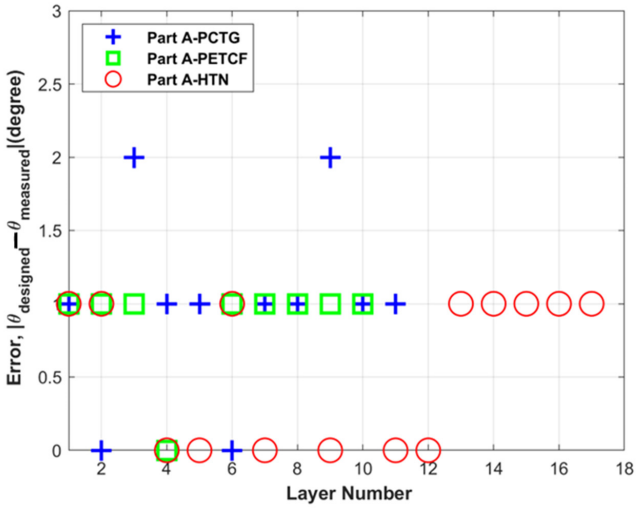

Figure 4. Errors against the number of layers for all parts with sample type A scanned with 10 MHz transducer.

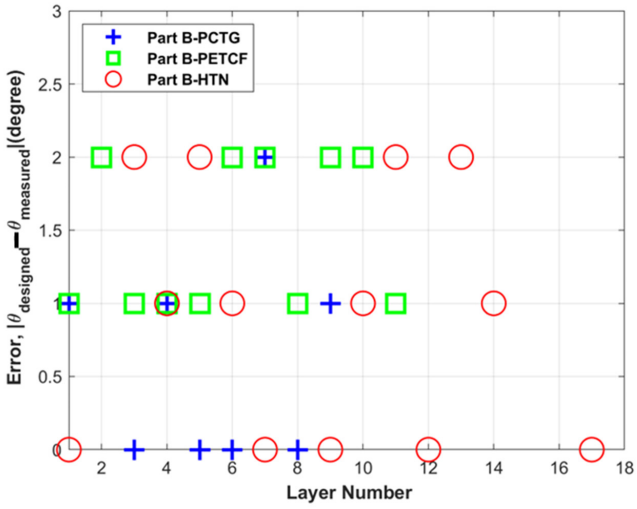

(**a**)

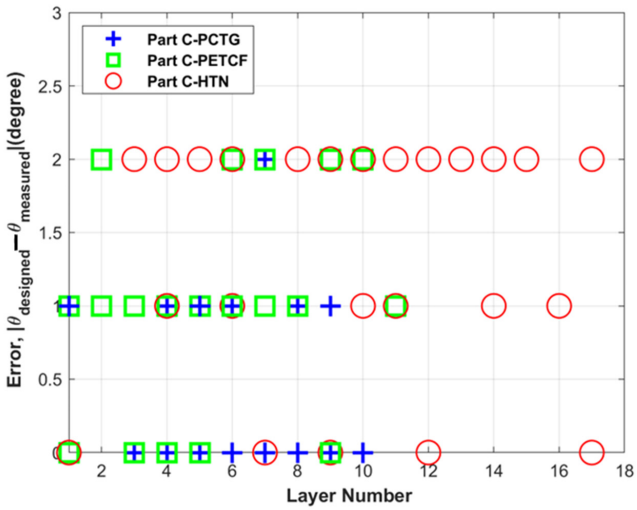

(**b**)

Figure 5. Errors against the number of layers for all parts with (**a**) sample type B and (**b**) sample type C scanned with 10 MHz transducer.

5. Conclusions

The as-manufactured performance of a 3D-printed part depends on the internal raster orientations. This paper presents a methodology using non-destructive means to identify the raster orientation. Three different part types were manufactured on an industrial 3D-fused filament fabrication printer, specifically the Essentium HSE 180, and three different material systems were studied. An algorithm utilizing the 2D FFT method was presented in which the raster orientation on a layer-by-layer basis could be extracted from the full acoustic waveform captured using pulse-echo ultrasound. The automated process consisted of extracting each layer using a C-scan based on the energy of the acoustic signal from reflections between layers and then performing a spatial two-dimensional Fourier transform of the data to generate the spatial frequency for the raster orientation extraction. The technique applied in this study can accurately detect the first 9~10 layers of the test coupons manufactured with PCTG and PET-CF with a typical error of 1°–2°. The inspection results for test coupons prepared with an engineered resin, specifically a high-temperature nylon, yielded the automated extraction of the raster orientation for the first 14 layers with the same error margin. This automated approach allows for quantifiable inspection of FFF components while limiting human error and allowing for the quantification of uncertainty in future studies that can be decoupled from the operator. This work also gives insights into the viability of UT as an inspection method for a variety of FFF materials. In terms of the limitations of the approach, it should be noted that during the investigation of the captured waveform, anomalies were observed in the peaks near the front surfaces of the parts. Additionally, the algorithm is specifically applied to materials with predetermined raster heights and thicknesses. Future studies will seek to identify the optimal set of parameters as well as methods to improve the signal-to-noise ratio of the captured acoustic waveform.

Author Contributions: For this research, A.A., D.A.J. and T.J.F. contributed to conceptualization, methodology, formal analysis, validation, and writing—original draft preparation. All authors have read and agreed to the published version of the manuscript.

Funding: This research received no external funding.

Institutional Review Board Statement: Not Applicable as studies do not involve humans or animals.

Informed Consent Statement: Not applicable.

Data Availability Statement: Data will be made available upon request to the corresponding author.

Acknowledgments: The authors would like to thank Baylor University for the financial support of this research.

Conflicts of Interest: The authors declare no conflicts of interest.

References

1. Ahn, S.H.; Montero, M.; Odell, D.; Roundy, S.; Wright, P.K. Anisotropic material properties of fused deposition modeling ABS. *Rapid Prototyp. J.* **2002**, *8*, 248–257. [CrossRef]
2. Sood, A.K.; Ohdar, R.K.; Mahapatra, S.S. Parametric appraisal of mechanical property of fused deposition modelling processed parts. *Mater. Des.* **2010**, *31*, 287–295. [CrossRef]
3. Wu, W.; Geng, P.; Li, G.; Zhao, D.; Zhang, H.; Zhao, J. Influence of layer thickness and raster angle on the mechanical properties of 3D-printed PEEK and a comparative mechanical study between PEEK and ABS. *Materials* **2015**, *8*, 5834–5846. [CrossRef] [PubMed]
4. Vega, V.; Clements, J.; Lam, T.; Abad, A.; Fritz, B.; Ula, N.; Es-Said, O.S. The effect of layer orientation on the mechanical properties and microstructure of a polymer. *J. Mater. Eng. Perfom.* **2011**, *20*, 978–988. [CrossRef]
5. Huang, B.; Singamneni, S. Raster angle mechanics in fused deposition modelling. *J. Compos. Mater.* **2015**, *49*, 363–383. [CrossRef]
6. Dudescu, C.; Racz, L. Effects of Raster Orientation, Infill Rate and Infill Pattern on the Mechanical Properties of 3D Printed Materials. *ACTA Univ. Cibiniensis* **2017**, *69*, 23–30. [CrossRef]
7. Gopi Mohan, R.; Santhosh, K.; Iyer, R.V.; John, L.K.; Ramu, M. Comparative analysis of mechanical properties of FDM printed parts based on raster angles. *Mater. Today Proc.* **2021**, *47*, 4730–4734. [CrossRef]
8. Jap, N.S.; Pearce, G.M.; Hellier, A.K.; Russell, N.; Parr, W.C.; Walsh, W.R. The effect of raster orientation on the static and fatigue properties of filament deposited ABS polymer. *Int. J. Fatigue* **2019**, *124*, 328–337. [CrossRef]

9. Lorenzo-Bañuelos, M.; Díaz, A.; Cuesta, I.I. Influence of raster orientation on the determination of fracture properties of polypropylene thin components produced by additive manufacturing. *Theor. Appl. Fract. Mech.* **2020**, *107*, 102536. [CrossRef]
10. Bahrami, B.; Ayatollahi, M.R.; Sedighi, I.; Pérez, M.A.; Garcia-Granada, A.A. The effect of in-plane layer orientation on mixed-mode I-II fracture behavior of 3D-printed poly-carbonate specimens. *Eng. Fract. Mech.* **2020**, *231*, 107018. [CrossRef]
11. Nabavi-Kivi, A.; Ayatollahi, M.R.; Razavi, N. Investigating the effect of raster orientation on fracture behavior of 3D-printed ABS specimens under tension-tear loading. *Eur. J. Mech.* **2023**, *99*, 104944. [CrossRef]
12. Kiendl, J.; Gao, C. Controlling toughness and strength of FDM 3D-printed PLA components through the raster layup. *Compos. B Eng.* **2020**, *180*, 107562. [CrossRef]
13. Srinivasan Ganesh Iyer, S.; Keles, O. Effect of raster angle on mechanical properties of 3D printed short carbon fiber reinforced acrylonitrile butadiene styrene. *Compos. Commun.* **2022**, *32*, 101163. [CrossRef]
14. Khosravani, M.R.; Reinicke, T. Effects of raster layup and printing speed on strength of 3D-printed structural components. *Procedia Struct. Integr.* **2020**, *28*, 720–725. [CrossRef]
15. Prajapati, H.; Chalise, D.; Ravoori, D.; Taylor, R.M.; Jain, A. Improvement in build-direction thermal conductivity in extrusion-based polymer additive manufacturing through thermal annealing. *Addit. Manuf.* **2019**, *26*, 242–249. [CrossRef]
16. Yap, Y.L.; Toh, W.; Koneru, R.; Lin, K.; Yeoh, K.M.; Lim, C.M.; Zheng, G. A non-destructive experimental-cum-numerical methodology for the characterization of 3D-printed materials—Polycarbonate-acrylonitrile butadiene styrene (PC-ABS). *Mech. Mater.* **2019**, *132*, 121–133. [CrossRef]
17. Rahul, K.; Jack, D.A.; Smith, D.E. A statistical approach for failure analysis involving uncertainty in determining ply orientation. *Polym. Compos.* **2024**, *5*, 5192–5206. [CrossRef]
18. Ogunleye, R.O.; Rusnakova, S.; Zaludek, S.; Emebu, S. The Influence of Ply Stacking Sequence on Mechanical Properties of Carbon/Epoxy Composite Laminates. *Polymers* **2022**, *14*, 5566. [CrossRef] [PubMed]
19. Vasudevan, A.; Pandiyarajan, R.; Navin Kumar, B.; Vijayarangam, J. Effect of Kevlar Ply Orientation on Mechanical Characterization of Kevlar-Glass Fiber Laminated Composites. *IOP Conf. Ser. Mater. Sci. Eng.* **2020**, *988*, 012088. [CrossRef]
20. Ramezani, F.; Carbas, R.; Marques, E.A.S.; Ferreira, A.M.; Da Silva, L.F.M. Study on out-of-plane tensile strength of angle-plied reinforced hybrid CFRP laminates using thin-ply. *Mech. Adv. Mater. Struct.* **2023**, *31*, 2859–2872. [CrossRef]
21. Yuan, Y.; Yao, X.; Liu, B.; Yang, H.; Imtiaz, H. Failure modes and strength prediction of thin ply CFRP angle-ply laminates. *Compos. Struct.* **2017**, *176*, 729–735. [CrossRef]
22. Smith, R.A.; Clarke, B. Ultrasonic C-scan determination of ply stacking sequence in carbon-fibre composites. *Insight* **1994**, *36*, 741–747.
23. Hsu, D.K.; Fei, D.; Liu, Z.J. Ultrasonically mapping the ply layup of composite laminates. *Mater. Eval.* **2002**, *60*, 1099–1106.
24. Hsu, D.K.; Margetan, F.J. Examining Cfrp Laminate Layup with Contact-Mode Ultrasonic Measurements. *Adv. Compos. Lett.* **1993**, *2*, 2. [CrossRef]
25. Smith, R.A.; Nelson, L.J.; Mienczakowski, M.J.; Challis, R.E. Automated analysis and advanced defect characterization from ultrasonic scans of composites. *Insight Non-Destr. Test. Cond. Monit.* **2009**, *51*, 82–87.
26. Ambrozinski, L.; Mrowka, J.; O'Donnell, M.; Pelivanov, I. Detection and imaging of local ply angle in carbon fiber reinforced plastics using laser ultrasound and tilt filter processing. *Compos. Part A Appl. Sci. Manuf.* **2019**, *126*, 105581. [CrossRef]
27. Kidangan, R.T.; Unnikrishnakurup, S.; Krishnamurthy, C.V.; Balasubramaniam, K. Uncovering the hidden structure: A study on the feasibility of induction thermography for fiber orientation analysis in CFRP composites using 2D-FFT. *Compos. B Eng.* **2024**, *269*, 111107. [CrossRef]
28. Amin, A.; Jack, D.; Fleck, T. Nondestructive Quantification of Internal Raster Path for Additively Manufactured Components via Ultrasonic Testing. *Sci. Rep.* **2024**, *14*, 11416. [CrossRef] [PubMed]
29. Amin, A.; Jack, D.; Fleck, T. Quantitative Inspection of Internal Raster Orientation of Additively Manufactured Components via Ultrasonic Nondestructive Testing. SPE, ACCE Conference 2022, September 7–9. Available online: https://speautomotive.com/wp-content/uploads/2022/10/Quantitative-Inspection-of-Internal-Raster-Orientation-of-Additively-Manufactured-Components-via-Ultrasonic-Nondestructive-Testing.pdf (accessed on 20 May 2024).
30. Blackman, N.J.; Jack, D.A. Automated Characterization of the Ply Stacking Sequence of a Woven Carbon Fiber Composite Using Pulse-Echo Ultrasound. *J. Compos. Sci.* **2023**, *7*, 398. [CrossRef]
31. Essentium PCTG Technical Data Sheet. Available online: https://essentium.com/wp-content/uploads/2020/08/TDS-Essentium-PCTG_v1.0-Minus-3D.pdf (accessed on 20 May 2024).
32. Essentium HTN Technical Data Sheet. Available online: https://essentium.com/wp-content/uploads/2020/08/TDS-Essentium-HTN_v1.0-Minus-3D.pdf (accessed on 20 May 2024).
33. Essentium PET-CF Technical Data Sheet. Available online: https://essentium.com/wp-content/uploads/2020/11/TDS-Essentium-PET-CF_v1.1.pdf (accessed on 20 May 2024).